

Assessment of Martian dust lifting schemes in the MarsWRF model

Lulu Li¹, Chun Zhao¹, Tao Li¹, Xianghui Xue², Jing Xiao³, Zhaopeng Wu⁴, Sheng-Fu Lin⁵, Jiamin Xu¹, Yongxuan Zhao¹, and Chengyun Yang¹

¹University of Science and Technology of China

²School of Earth and Space Sciences, University of Science and Technology of China

³Space Science Institute, Macau University of Science & Technology

⁴Sun Yat-sen University

⁵USTC

December 21, 2022

Abstract

MarsWRF, the general circulation model of Mars, is one of the most commonly used models to study the dust cycle in the Martian atmosphere. It has been widely used to study the mechanisms of dust storms and their effects on the Martian atmosphere. To better understand the ability of MarsWRF to simulate the dust cycle on Mars, this study assesses the current dust lifting schemes in the model, specifically the convective lifting and wind stress schemes. It is found that, by tuning lifting efficiency, the model with the convective lifting scheme can generally reproduce the seasonal variation of the mid-level atmospheric temperature (T15) but cannot reproduce the observed spatial distribution of dust devils, which exhibits non-homogeneous (uniform) distribution in the northern (southern) hemisphere. The model with the wind stress lifting scheme can generally capture the observed magnitude of T15 and column dust optical depth (CDOD) with properly tuned lifting efficiency and threshold drag velocity. There is a discrepancy in the assessment of modeling seasonal variations of dust with T15 and CDOD, which may be partly due to the observational uncertainties related to T15 and CDOD and the empirical modeling methods of Martian dust optical properties and radiative effect. For the spatial distribution of dust, there are significant simulation biases regardless of the tuning, which may be caused by the biases in the dust lifting process and large-scale atmospheric circulation. The analysis highlights that dust lifting schemes need further improvement to better represent the dust cycle and their impacts on Mars.

Hosted file

951817_0_art_file_10536006_rmvzdg.docx available at <https://authorea.com/users/568277/articles/614200-assessment-of-martian-dust-lifting-schemes-in-the-marswrf-model>

Hosted file

951817_0_supp_10522141_rmmkm5.docx available at <https://authorea.com/users/568277/articles/614200-assessment-of-martian-dust-lifting-schemes-in-the-marswrf-model>

Assessment of Martian dust lifting schemes in the MarsWRF model

¹Lulu Li, ^{1,2}Chun Zhao*, ¹Tao Li, ¹Xianghui Xue, ³Jing Xiao, ⁴Zhaopeng Wu, ¹Shengfu Lin,
¹Jiamin Xu, ¹Yongxuan Zhao, ¹Chengyun Yang

¹Deep Space Exploration Laboratory / School of Earth and Space Sciences, University of Science and Technology of China, Hefei 230026, China

²CAS Center for Excellence in Comparative Planetology, University of Science and Technology of China, Hefei, China

³Space Science Institute / Lunar and Planetary Science Laboratory, Macau University of Science and Technology, Macau, China

⁴Institute of Geology and Geophysics / Key Laboratory of Earth and Planetary Physics, Chinese Academy of Science, Beijing, China

The manuscript for submission to *JGR-Planets*

*Corresponding author: Chun Zhao (chunzhao@ustc.edu.cn)

Three key points:

1. Current convective lifting scheme can reproduce seasonal variation of global mean dust but not observed spatial distribution of dust devils.
2. There is a discrepancy in the assessment of modeling seasonal variations of dust with T15 and CDOD with current wind stress lifting scheme.
3. Modeling biases in dust spatial distributions may be caused by the biases in lifting processes and large-scale atmospheric circulation.

28 **Abstract**

29 MarsWRF, the general circulation model of Mars, is one of the most commonly used
30 models to study the dust cycle in the Martian atmosphere. It has been widely used to study
31 the mechanisms of dust storms and their effects on the Martian atmosphere. To better
32 understand the ability of MarsWRF to simulate the dust cycle on Mars, this study assesses the
33 current dust lifting schemes in the model, specifically the convective lifting and wind stress
34 schemes. It is found that, by tuning lifting efficiency, the model with the convective lifting
35 scheme can generally reproduce the seasonal variation of the mid-level atmospheric
36 temperature (T15) but cannot reproduce the observed spatial distribution of dust devils,
37 which exhibits non-homogeneous (uniform) distribution in the northern (southern)
38 hemisphere. The model with the wind stress lifting scheme can generally capture the
39 observed magnitude of T15 and column dust optical depth (CDOD) with properly tuned
40 lifting efficiency and threshold drag velocity. There is a discrepancy in the assessment of
41 modeling seasonal variations of dust with T15 and CDOD, which may be partly due to the
42 observational uncertainties related to T15 and CDOD and the empirical modeling methods of
43 Martian dust optical properties and radiative effect. For the spatial distribution of dust, there
44 are significant simulation biases regardless of the tuning, which may be caused by the biases
45 in the dust lifting process and large-scale atmospheric circulation. The analysis highlights that
46 dust lifting schemes need further improvement to better represent the dust cycle and their
47 impacts on Mars.

48

49

50 **Plain Language Summary**

51 Numerical models are important tools to study the dust cycle on Mars, but the ability of
52 current numerical models to simulate the Martian atmospheric dust amount is still not very
53 clear. Therefore, this study evaluates two dust lifting schemes in the widely used Martian
54 model MarsWRF, i.e., the convective lifting scheme and wind stress lifting scheme. The
55 model with the convective lifting scheme can reproduce the seasonal variation of the air
56 temperature but cannot well reproduce the spatial distribution of convective processes that
57 cause dust uplift. The model with the wind stress lifting scheme can capture the magnitude of
58 air temperature and dust optical depth. However, there is a discrepancy in the assessment of
59 simulated seasonal variation of dust with temperature and dust optical depth, which may be
60 partly due to the observational uncertainties and the biases of modeling dust optical
61 properties. There are also large modeling biases in the dust spatial distribution that may be
62 related to the deficiency of the dust lifting process and large-scale atmospheric circulation
63 around the polar region. The study brings some new perspectives on the assessment of dust
64 lifting schemes and raises some problems to be solved.

65
66
67
68
69

70 1. Introduction

71 According to early observations (Capen & Martin, 1971; McKim, 1999), the yellow
72 clouds observed by the telescope indicated the presence of dust in the Martian atmosphere.
73 On Mars, dust is of significant importance to the Martian atmosphere, analogous to the
74 importance of water to the Earth's atmosphere (Wu et al., 2022). The spatial and temporal
75 distributions of dust are particularly important for the Martian atmosphere because dust in the
76 atmosphere can interact with solar and infrared radiation (Haberle et al., 2017; Kahre et al.,
77 2006; Pollack et al., 1990). The presence of airborne dust affects the atmospheric heating rate,
78 which drives dynamic processes, so the presence of atmospheric dust strongly affects the
79 circulation (Gierasch & Goody, 1968; Haberle et al., 1982).

80 According to the position of Mars to the sun (solar longitude, Ls), four seasons can be
81 recognized on Mars: spring (Ls of 0–90°), summer (Ls of 90– 180°), autumn (Ls of 180–
82 270°) and winter (Ls of 270– 360°). The general annual repeatability of the change in dust
83 mass loading with the seasons constitutes the dust cycle in a year, which is characterized by
84 the "non-dusty season" (Ls~0–135°) and the "dusty season" (Ls~135– 360°) (Kahre et al.,
85 2017). "Non-dusty season" (Ls~0–135°) includes northern spring and early summer. During
86 this season, the value of column dust opacity is relatively small except at high latitudes.
87 According to the image data from Viking, MGS, MRO, and MEX, there is locally higher dust
88 opacity near the edges of the seasonal CO₂ caps, caused by the enhanced winds related to
89 topography and pressure variation that is related to the retreatment of two seasonal polar cap
90 edges (Cantor et al., 2001; James et al., 1999). The "dusty season" (Ls~135– 360°) includes
91 northern autumn and winter. Large-scale dust storms can often be observed during the "dusty
92 season". During this time, dust storms on Mars were observed to exhibit various sizes and
93 durations. Local dust storms (surface areas < $1.6 \times 10^6 km^2$ and lasting less than 2 sols) are
94 the most frequently observed storms throughout the Martian year, mainly occurring near the
95 edges of polar caps and the mid-latitude regions of both hemispheres (Cantor et al., 2002;
96 2010; 2001; Kahre et al., 2017; Toigo et al., 2018). Based on the image of Mars Global
97 Surveyor MARS Orbiter Camera (MOC), regional dust storms (surface areas $\geq 1.6 \times$
98 $10^6 km^2$ and lasting more than 2 sols) occur about 8-35 times during Ls~130-160° and
99 Ls~330-20° per year (Cantor, 2007; 2001). Most regional dust storms are caused by the
100 merging of multiple local storms, loading more dust into the atmosphere and increasing the
101 atmospheric temperature. Global-scale dust storms (GDSs), consisting of two to three
102 regional dust storms, are the major atmospheric events lasting from several weeks to months

103 in the Martian atmosphere. According to observations by spacecraft and telescopes, most
104 GDSs occur every 2 to 3 Martian years and cover almost all longitudes of both hemispheres
105 (Basu et al., 2006; Bertrand et al., 2020; Viúdez - Moreiras et al., 2019; Zurek & Martin,
106 1993).

107 Since Gierasch and Goody (1972) first showed that observed dust has a significant effect
108 on the thermal state of the Martian atmosphere, numerical models have been used to study
109 the Martian dust cycle. These models are developed following the models of the Earth. The
110 mechanisms of dust injection into the Martian atmosphere are challenging for developing
111 Martian GCMs. There have been many studies focusing on the parameterization of dust
112 lifting in the model (Merrison et al., 2007; Newman & Richardson, 2015). Wilson &
113 Hamilton (1996) implemented a dust injection scheme based on the heat and momentum
114 exchange between the surface and the atmosphere. With the scheme, the model can
115 successfully simulate the seasonal cycle of dust opacities compared to the observations from
116 Mariner-9 and Viking, although global dust storms cannot be simulated. Later, Newman et al.
117 (2002a, 2002b) developed a new set of active dust injection schemes, which can deepen the
118 understanding of the dust life cycle and its impacts on the atmospheric state. The model with
119 these schemes can also produce regional dust storms to some extent. Kahre et al. (2006)
120 compared a modified Earth-based dust lifting mechanism (Westphal et al., 1987) for the
121 Martian environment and the mechanism proposed by Newman et al. (2002b). They found
122 that both can reproduce the dust cycle in a nonglobal dust storm year, as observed by TES.

123 So far, the two schemes proposed by Newman et al. (2002b) are most commonly used in
124 the model for dust lifting. The first is the lifting of dust caused by surface wind stress, which
125 only occurs when the surface stress is greater than an estimated threshold, including the
126 saltation of sand (larger dust particles with diameters greater than 20 μm) and the suspension
127 of smaller dust particles (diameter smaller than 20 μm) (Greeley & Iversen, 1987). Previous
128 studies indicated that dust could be lifted by the saltation of sand particles when wind speeds
129 on Mars are far below the wind stress of dust particles (Newman et al., 2002b; Pollack et al.,
130 1976). Although sand particles are too heavy to remain aloft in the Martian atmosphere even
131 if background vertical winds blow them up, the saltation of sand particles to the surface
132 quickly increases the surface stress, which leads to dust particles being lifted more easily.
133 The second is the lifting of dust by convective vortices (sometimes namely, dust devils),
134 caused by the large pressure gradient and high tangential wind around the vortex core. Dust
135 devils have been observed in the images taken by Viking Orbiter Cameras (Thomas &

136 Gierasch, 1985) and the MOC with different sizes and different durations Cantor et al., 2006;
137 Fisher et al., 2005; Whelley & Greeley, 2006; 2008). They are mainly concentrated in the
138 spring and summer seasons of the two hemispheres. Since the horizontal scales of the
139 convective vortex are approximately a few centimeters to hundreds of meters and the vertical
140 scale is up to the top of the convective boundary layer, the dust lifting process caused by the
141 convective vortex occurs more easily than that caused by surface wind stress.

142 Understanding the effects of dust on the Martian atmosphere requires accurate spatial
143 and temporal distributions of atmospheric dust. Previous studies showed that different
144 combinations of dust lifting schemes could be adjusted to obtain reasonable dust opacity
145 throughout a Martian year compared to the observations. Kahre et al. (2006), using the
146 NASA Ames Mars GCM, suggested that the contributions from convective lifting and wind
147 stress lifting were equal to the total dust mass loading in a Martian year without global dust
148 storms. Whelley and Greeley (2008), based on the MOC images, suggested that the dust flux
149 lifted by the convective process should be half of that lifted by near-surface wind stress.
150 Newman et al. (2005) showed that the contribution of convective lifting was not as large as
151 illustrated by previous studies, although they did not provide an exact ratio. Using different
152 models and different environment settings, different relative contributions of the two lifting
153 processes may be obtained.

154 So far, the contributions of the two dust lifting schemes are still uncertain because a few
155 parameters related to the lifting efficiency and threshold in the schemes cannot be constrained
156 with direct observations; instead, they are often tuned by indirect observations. For example,
157 most previous studies adjusted these parameters mainly to produce a reasonable atmospheric
158 temperature. Basu et al. (2004) simulated dust cycles over several Martian years without
159 global dust storms. They were able to produce a global mean atmospheric temperature highly
160 similar to the observations in spring and summer by adjusting the parameters in the two dust
161 lifting schemes. However, the tuning parameters cannot be sufficiently constrained by
162 atmospheric temperature alone. In addition, it is also necessary to evaluate the performance
163 of individual lifting schemes and understand their deficiencies rather than evaluating the
164 combined performance of the two lifting schemes. Therefore, in this study, two fields,
165 atmospheric temperature and column dust optical depth (CDOD), are used together to
166 provide a comprehensive assessment of the two dust lifting schemes in a Mars GCM. Both
167 the temporal and spatial characteristics of the focused fields are examined. Section 2
168 introduces the MarsWRF GCM employed for this study. The design of the experiments and
169 data used are also described. Section 3.1 evaluates the convective lifting scheme using

170 temperature and the spatial distribution of dust devils. Section 3.2 shows the evaluation of the
171 wind stress lifting scheme from temporal and spatial distributions by using temperature and
172 CDOD. The conclusion and discussion are shown in Section 4.

173

174 **2. Methodology**

175 **2.1 Model and experiments**

176 2.1.1 MarsWRF

177 MarsWRF is a three-dimensional (3-D) numerical model for the Martian atmosphere
178 developed based on the Weather Research and Forecasting (WRF) mesoscale model for the
179 Earth (Guzewich et al., 2013; Richardson et al., 2007; Toigo et al., 2012). Atmospheric
180 processes can be examined by MarsWRF at various resolutions from the microscale to
181 global-scale (Fenton & Richardson, 2001; Hinson & Wilson, 2002; Wu et al., 2021; Xiao et
182 al., 2019).

183 The processes related to the dust life cycle in this model include dust lifting into the
184 atmosphere, vertical mixing and diffusion, horizontal advection, and sedimentation. Dust
185 lifted into the air can lead to radiative effect on the atmosphere at both solar and thermal
186 infrared wavelengths. Therefore, a reasonable simulation of the spatial and temporal
187 distributions of atmospheric dust is crucial to understanding the thermal and dynamic
188 structures of the Martian atmosphere.

189

190 2.1.2 Dust scheme

191 To simulate the dust life cycle and its impact on the atmosphere, the dust lifting process
192 from the surface into the atmosphere should be simulated properly. This study investigates
193 two dust lifting schemes available in MarsWRF (Newman et al. (2002b): the convective
194 lifting scheme (Section 2.1.2.1) and the near-surface wind stress lifting scheme (Section
195 2.1.2.2). The mechanisms of these two schemes, their formulation and the relevant tuning
196 parameters are described below.

197

198 2.1.2.1 Convective Lifting

199 The convective lifting of dust results from atmospheric vortices that exist not only on
200 Earth but also on Mars. Martian convective lifting of dust (dust devil) can be seen through
201 Viking Orbiter Camera images (Thomas & Gierasch, 1985) and Mars Global Surveyor Mars
202 Orbiter Camera images (Cantor et al., 2001). The low pressure in the center of the dust devil,

203 surrounded by strong tangential winds and a vertical upward velocity structure, can
 204 effectively suck in dust from the surface up to the top of the convective boundary layer. This
 205 process is generally small-scale, contributing to the small dust particles in the Martian
 206 atmosphere.

207 Rennó et al. (1998) developed a parameterization of the small-scale convective motion
 208 of dust based on thermodynamic theory, and Newman et al. (2002b) implemented it in
 209 MarsWRF. The convective lifting flux of dust is defined as

$$210 \quad F_{CL} = \alpha_{CL} \cdot F_s \cdot \eta, \quad (1)$$

211 α_{CL} is a tunable efficiency parameter for convective lifting with units of $kg J^{-1}$, F_s is the
 212 sensible heat flux ($W m^{-2}$), and η is the thermodynamic efficiency, which is given by $1 - b$,
 213 where

$$214 \quad b = \frac{p_s^{\chi+1} - p_{top}^{\chi+1}}{(p_s - p_{top})(\chi+1)p_s^\chi}, \quad (2)$$

215 where p_s is the surface pressure (Pa), p_{top} is the pressure at the top of the convective
 216 boundary layer (Pa), and χ is the specific gas constant divided by the specific heat capacity at
 217 constant pressure. According to Eq. 2, it can be seen that η increases with the height of the
 218 convective boundary layer.

219 In this convective lifting scheme, dust can be lifted as long as the upward heat flux at the
 220 surface is positive regardless of the dust particle size. At noon and afternoon, the solar
 221 radiation received by the surface increases, and consequently, the upward heat flux at the
 222 surface increases, which leads to an increase in the convective lifting flux.

223

224 2.1.2.2 Wind Stress Lifting

225 In addition to being lifted up by convective processes, dust can be blown into the
 226 atmosphere by near-surface wind stress. In the wind stress lifting scheme, a wind stress
 227 threshold is needed to determine the occurrence of dust events. In general, only very
 228 unfeasible high surface winds can lift dust particles at micron or smaller scales directly into
 229 the air (Bagnold, 1974). Instead, a steady movement of sand-sized particles ($\sim 100 \mu m$) (i.e.,
 230 saltation) can occur even under conditions with small wind speeds, increasing the near-
 231 surface wind stress by the saltating sand particles and lifting the surface dust. Therefore, the
 232 threshold at which the initial saltation can occur to make the sand move is the key to
 233 determining the wind stress lifting of dust. This threshold for sand-sized particle movement is
 234 calculated in MarsWRF as follows.

235 In the MarsWRF, the wind stress threshold τ_* ($\tau_* = \rho(u_{drag}^t)^2$) is a function of the
 236 threshold drag velocity (u_{drag}^t). Dust can only be lifted when the actual drag velocity, u_{drag} ,
 237 is greater than u_{drag}^t . The wind stress lifting scheme based on the saltation theory used in this
 238 study was formulated by White (1979). The magnitude of the vertical dust flux (F_{SL}) lifted
 239 from the surface is defined as

$$240 \quad F_{SL} = \alpha_{SL} \cdot 2.61 \frac{\rho}{g} (u_{drag})^3 \left(1 - \frac{u_{drag}^t}{u_{drag}}\right) \left(1 + \frac{u_{drag}^t}{u_{drag}}\right)^2, \quad (3)$$

241 where α_{SL} is a tunable constant named the ‘‘lifting efficiency’’, ρ is the atmospheric density
 242 (kg m^{-3}), and g is the Martian gravity (m s^{-2}). The frictional wind speed in the atmospheric
 243 boundary layer proposed by Garratt (1994) is calculated as follows:

$$244 \quad u_{drag} = \frac{ku(z)}{\ln\left(\frac{z}{z_0}\right)}, \quad (4)$$

245 where k is the von Karman constant, z is the height above the surface (m) and z_0 is the
 246 aerodynamic roughness length, taken as 0.01 m.

247 u_{drag}^t can be calculated by $\sqrt{\frac{\tau_*}{\rho}}$, with a constant τ_* or calculated with a semi-empirical
 248 formula:

$$249 \quad u_{drag}^t = \beta \cdot A \sqrt{g D_P \frac{\rho_d}{\rho}}, \quad (5)$$

250 where D_P is the diameter of the dust ($\sim 4\mu\text{m}$), ρ_d is the dust density of approximately 2500
 251 kg m^{-3} , and A is a semi-empirical function of the friction Reynolds number that is defined as
 252 (using the formula in Newman et al. (2002b) here). Different surface roughness values will
 253 result in different friction Reynolds numbers and thus lead to different possibilities of dust
 254 lifting. The friction Reynolds number generally increases with the roughness of the surface.
 255 This study introduces a tunable coefficient β to account for the uncertainties of u_{drag}^t , and
 256 the default value is 1.0. More details about the formulas of wind stress lifting can be found in
 257 Newman et al. (2002a).

258

259 2.2 Numerical Experiments

260 All the experiments in this work are conducted at the global scale, where MarsWRF acts
 261 as a general circulation model (GCM). In this study, the global domain of MarsWRF has a
 262 horizontal spatial resolution of 5 degrees (36 latitude \times 72 longitude grid points), with 52
 263 vertical levels of non-uniform thickness located between the surface and the model top about
 264 80 km in altitude. The model includes the treatment of topography derived from the Mars

265 Orbiter Laser Altimeter (MOLA); thermal inertia and albedo maps derived from Viking and
266 Thermal Emission Spectrometer (TES) data; the CO_2 cycle, including the seasonal variations
267 of the two polar ice caps; and the dust cycle and radiative interactions with dust and CO_2 in
268 the visible and thermal infrared. None of the experiments in this work consider the presence
269 of water vapor.

270 Sensitivity experiments of three parameters show that they can impact the dust lifting
271 processes. The first one is lifting efficiency, α_{CL} , in the convective lifting scheme (Eq. 1).
272 The other two free parameters can modulate the dust lifting flux in the wind stress lifting
273 scheme (Eq. 3): lifting efficiency (α_{SL}) and threshold drag velocity (u_{drag}^t). In this study,
274 u_{drag}^t is tuned by changing β . All the experiments conducted in this study are summarized in
275 Table 1. The experiments of CL1, CL2, and CL3 are conducted by tuning the parameter α_{CL}
276 in the convective lifting scheme to values of 1, 3, and 10 ($\times 10^{-9} kg J^{-1}$), respectively. For
277 the wind stress lifting scheme, two parameters can be changed. To prevent them from
278 affecting each other, in the experiments of SL1, SL2, and SL3, α_{SL} is set to the same value of
279 $5 \times 10^{-7} m^{-1}$ and β is changed to the values of 1, 0.35, and 0.1, respectively. Experiments
280 with fixed β but changing α_{SL} are not conducted and discussed in this study, but the effect is
281 similar. The values of α_{CL} and β are selected intentionally to cover all the probability of dust
282 distribution that may occur. CAP and SL2 use the same settings except that the lifting
283 efficiency in CAP is increased to $5 \times 10^{-6} m^{-1}$ ($4 \times 10^{-5} m^{-1}$) near the southern (northern)
284 ice cap once CO_2 ice sublimation occurs in the past 30 sols. All experiments are run for one
285 Martian year that does not include global-scale dust storms. The simulations are cycled for
286 two years. The first year of simulation is treated as a spin-up, and the simulation results for
287 the second year are analyzed.

288

289 **2.3 Observation and reanalysis datasets**

290 As mentioned above, the aim of this study is to improve our understanding of physical
291 processes in the Martian dust cycle by re-evaluating the wind stress lifting scheme and
292 convective lifting scheme using multiple observational datasets. In recent decades, Martian
293 atmospheric conditions have been constantly detected by spacecraft and ground-based
294 observations. The observations of Martian temperature and dust optical depth can be obtained.
295 Montabone et al. (2015) obtained a multiannual climatology of the column dust optical depth
296 dataset (referred to as the LMD dataset below) using observations of the Martian atmosphere
297 from MY24 to MY34 by different orbiting instruments. The observations for eight Martian

298 years without global-scale dust storms represent the climatology of Martian dust and are used
299 to evaluate the accuracy of the simulated dust cycle. In addition, the CDOD and temperature
300 of the climatology scenario (with non-global dust storms) in the Mars Climate Database,
301 version 5.3 (MCD v5.3), a database of meteorological fields derived from state-of-the-art
302 Martian GCM numerical simulations and validated using available observational data, are
303 also used (Forget et al., 1999; Madeleine et al., 2011).

304

305 **3. Results**

306 **3.1 Convective lifting process**

307 To examine the performance of the convective lifting scheme of dust, three experiments
308 with the convective lifting process only are conducted by adjusting the sensitivity coefficient
309 α_{CL} to modulate dust emission fluxes, and the specific adjustment of α_{CL} is shown in Table 1.
310 According to the seasonal variation of zonal-mean dust lifting flux shown in Figure 1, α_{CL}
311 increases gradually from CL1 to CL3, which corresponds to a rise in the amount of dust
312 injected into the air, especially around $30^{\circ}N$ in spring and summer in the northern
313 hemisphere, and around $30^{\circ}S$ in spring and summer in the southern hemisphere. The large
314 value of dust lifting is near $30^{\circ}N$ ($30^{\circ}S$) in the spring and summer corresponding to both
315 hemispheres, which is related to solar radiation. Because of the large eccentricity of Mars
316 compared to the Earth, Mars is near the perihelion of the Sun during the spring and summer
317 in the southern hemisphere, resulting in much more solar radiation being received during that
318 period than during the aphelion of Mars.

319 In some previous studies (Basu et al., 2004; Newman & Richardson, 2015), the
320 brightness temperature of the 15- μm channel derived from the Viking Orbiter IRTM is
321 preferred to assess the realism of dust loading due to the dust radiative effect in the
322 atmosphere. Therefore, T15 refers to the brightness temperature of the IRTM 15- μm channel
323 or the temperature calculated from the corresponding IRTM 15- μm channel weighting
324 function, which mainly reflects the temperature at altitudes of 10-40 km (centered at ~ 25 km
325 or ~ 50 Pa) between the latitudes of $40^{\circ}S$ and $40^{\circ}N$. The use of T15 to evaluate the model is
326 based on the assumption that when the simulated results are close to the observed air
327 temperature, the simulated dust distribution is considered reasonable. Figure 2 shows the
328 seasonal magnitude and variation of T15. In Figure 2a, the magnitude of T15 in the left panel
329 shows that as α_{CL} increases, the increase of dust amount in the atmosphere leads to the
330 strengthening of atmospheric warming. All three experiments reflect that T15 shows the

331 seasonal cycle of low temperature in boreal spring and summer and high temperature in
332 autumn and winter. In the three experiments, the T15 in CL2 is the closest to that in MCD,
333 especially in boreal spring and summer. This indicates that the temperature variation in
334 boreal spring and summer can be well simulated using the convective lifting scheme only,
335 and there is a slight underestimation for autumn. To better study the seasonal variation of
336 temperature, the normalized T15 is calculated by dividing it by its maximum value in the
337 year. As seen from the normalization of T15 in the right panel, the seasonal variation in T15
338 can be simulated using the convective lifting scheme alone, and the pattern of the seasonal
339 variation is similar regardless of α_{CL} .

340 The dust devil is a vortex motion that causes dust uplift as the main contributor to
341 convective lifting. The convective lifting scheme is developed based on the thermodynamic
342 theory of dust devils to reproduce the background dust caused by this process. However, the
343 comparison with observations reveals that there are still large caveats in this scheme. Cantor
344 et al. (2006) showed that the dust devils observed by MOC are mainly concentrated in the
345 latitude range from $71.9^{\circ}S$ to $62.2^{\circ}N$. They also showed the distribution characteristics of
346 more dust devils in the northern hemisphere (about 88.5%) and less in the southern
347 hemisphere. The distribution of dust devils in the northern hemisphere is uneven, with the
348 majority of dust devils concentrated near Amazonis Planitia. The observed dust devils in the
349 southern hemisphere are much less than those in the northern hemisphere, but the distribution
350 is uniform.

351 The spatial distribution of the dust lifting flux caused by convective processes can be
352 seen in Figure 3a. The simulated results with convective processes can generally reflect the
353 spatial distribution of lifting dust associated with dust devils. The dust lifting fluxes are the
354 largest in the northern Amazonis Planitia relative to other regions. In comparison, the
355 distribution of dust lifting fluxes in the southern hemisphere is more uniform. Although the
356 convective lifting fluxes show a similar spatial distribution as above, the lifting fluxes and the
357 number of dust devils are significantly different. Therefore, this study also compares the
358 simulated frequency of convective lifting with observations. When the convective lifting flux
359 of dust is greater than zero, it is considered a dust devil event. The frequency of dust devils is
360 obtained by accumulating the number of dust devils and dividing by the total number of days
361 in a Martian year. If the frequency is closer to 1, it indicates that the dust devil has a greater
362 probability of occurring, closer to the occurrence once a day, and on the other hand, it means
363 no dust devil event occurred when the frequency is closer to 0. The spatial distribution of the

364 frequency of dust devils (Figure 3b) shows that the frequency of dust devils in the mid-
365 latitudes of the two hemispheres is close to 1 and is reduced near the equator and high
366 latitudes. The dust devils in the middle latitudes of the northern hemisphere are uneven, and
367 there are three areas with a larger frequency of dust devils, while the distribution of dust
368 devils in the southern hemisphere is more uniform. However, compared with the observation,
369 there are two problems. First, the number of dust devils near Amazonis Planitia in the
370 northern hemisphere observed by MOC is the largest (Cantor et al., 2006), but the three
371 simulated areas of high values of dust devil occurrence do not include northern Amazonis
372 Planitia. Second, there are more dust devils in the mid-latitudes in the southern hemisphere
373 than in the northern hemisphere, which is also inconsistent with observations. The discussion
374 above illustrates that although the model with the current convective lifting scheme can be
375 tuned to capture the observed seasonal variation of global mean atmospheric temperature, it
376 cannot reproduce the non-uniform spatial and temporal distribution of dust devils. This is
377 mainly because dust devils can occur anywhere in the current model as long as there are
378 processes of heat transport from the surface to the near-surface atmosphere, which deviates
379 from the observed spatial distribution of the occurrence frequency of dust devils.

380

381 **3.2 Wind stress lifting process**

382 3.2.1 Seasonal variation

383 As discussed above, the convective lifting scheme has evident caveats, so can the model
384 produce general features of the dust life cycle with the wind stress lifting scheme only and to
385 what extent? This is focused on in the analysis below. Figure 4a shows the spatial distribution
386 of the dust lifting flux caused by the near-surface wind stress lifting process. Only a few dust
387 particles lifted in the northern hemisphere during autumn and winter, and almost no dust was
388 lifted in other seasons. This is mainly because the threshold drag velocity (u_{drag}^t) prescribed
389 in the model may be too high. Therefore, u_{drag}^t is reduced in the sensitivity experiments (as
390 described above in Section 2.2), and the corresponding simulation results are shown in Figure
391 4b and Figure 4c. With decreasing u_{drag}^t from SL1 to SL3, the dust lifting is significantly
392 enhanced, with total lifting masses of 2.85×10^{12} , 1.93×10^{14} and 4.87×10^{14} kg,
393 respectively. In the spring and summer of the northern hemisphere (especially near $30^\circ N$)
394 and that of the southern hemisphere (near $30^\circ S$), the dust mass lifted into the atmosphere
395 increases. The two dust lifting centers ($Ls=180^\circ$ and $Ls=0^\circ$) in the area near $30^\circ N$ become

396 more evident with the decrease of the threshold drag velocity. In addition, the uplift dust flux
397 at the receding edge of the Antarctic ice cap has also increased significantly.

398 The change of u_{drag}^t affects the simulated dust concentration and thus changes the
399 temperature in the Martian atmosphere. Figure 5 shows the seasonal variation of T15
400 simulated by these three experiences. It can be seen that the injected dust amount from SL1 to
401 SL3 keeps increasing, leading to an improvement of the simulated T15 against the
402 observation. Among the three experiments, T15 in SL2 is the closest to the observations,
403 especially in boreal spring and summer, with a slight overestimation in boreal winter. The
404 simulated T15 in SL3 is about 10 K higher than that in MCD throughout the year. SL1
405 significantly underestimates T15. After normalizing T15 (Fig. 5b), the seasonal variation in
406 SL1 is small because a high threshold drag velocity prohibits dust lifting from the wind stress
407 process throughout the year globally. Interestingly, the seasonal variation of the simulated
408 T15 in SL3 is better than that in SL2, mainly reflected by the relative overestimation of T15
409 in boreal winter in SL2.

410 Previous studies suggested that it is necessary to combine convective lifting and wind
411 stress lifting schemes to capture the temporal variation of T15. This is because the threshold
412 drag velocity is set too large to lift dust through the wind stress process that is only allowed
413 to occur in specific regions and seasons. To compensate for the underestimation of lifted dust
414 from the wind stress process, previous studies applied the current convective scheme to
415 capture the global mean atmospheric temperature. However, as discussed above, the current
416 convective scheme cannot produce a reasonable spatial distribution of the observed
417 occurrence of dust devils. According to Fig. 5, it is possible to reproduce the seasonal
418 magnitude and variation of T15 using the wind stress lifting scheme only with tuned
419 parameters.

420 In addition to T15, which is often used to assess the accuracy of Martian dust simulation,
421 dust optical depth (DOD) is another important metric to assess simulated dust. However,
422 most previous studies chose only one of the two for the evaluation (Basu et al., 2004; Kahre
423 et al., 2006; Newman et al., 2002a). In this study, the assessments with both are compared.
424 The seasonal magnitude and variation of the global average column integrated DOD (CDOD)
425 are shown in Figure 6. According to the left panel, the observed CDOD shows consistent dust
426 seasonal variation as reflected by T15, i.e., less dust in boreal spring and summer and more
427 dust in boreal autumn and winter. In addition, there are two peaks in autumn and winter, with
428 the main peak roughly between $L_s = 200^\circ - 270^\circ$, where the observed CDOD can reach a

429 maximum of 0.3, and a weaker peak between $L_s = 315^\circ - 340^\circ$. The CDOD in SL1 is very
430 small throughout the year. After normalization, the seasonal variation of CDOD in SL1 can
431 also be seen, but its value in spring and summer is significantly underestimated. The CDOD
432 in SL2 is the closest to the observations among all three experiments in magnitude and
433 variation, particularly in spring and summer. Consistent with that reflected by T15, SL3
434 overestimates CDOD throughout the year. In addition, it also relatively overestimates the
435 CDOD in spring and summer, which is not in line with its performance on T15. All the
436 experiments cannot capture the two peaks shown in the MCD reanalysis dataset. This may be
437 partly due to that large dust particles are quickly settled down in the current model with only
438 one dust particle size (Wang et al., 2021), which deserves further investigation.

439 According to the assessment with CDOD, the performance of SL2 seems to capture the
440 observed seasonal magnitude and variation of global mean dust well and overwhelm the other
441 two experiments. However, according to Fig. 5, SL2 seems to relatively overestimate T15 in
442 boreal winter. One reason for the discrepancy may be due to the sampling inconsistency of
443 T15 and CDOD in the dataset. As mentioned above, T15 reflects the temperature at altitudes
444 of 10-40 km (centered at ~ 25 km or ~ 50 Pa) between the latitudes of $40^\circ S$ and $40^\circ N$, while
445 CDOD reflects the global mean dust at all heights. The global average atmospheric
446 temperature at altitudes of 10-40 km and altitudes of up to 80 km is shown in Figure S1 and
447 Figure S2, respectively (in the supporting material). SL2 still relatively underestimates the
448 temperature in spring and summer. Therefore, the inconsistency between the assessment of
449 SL2 with T15 and CDOD cannot be attributed to sampling differences in T15 and CDOD.
450 There may be two reasons for the inconsistency. One is the observational uncertainties
451 related to T15 and CDOD, which may deserve further investigation about the retrieval or
452 assimilation methods. Another reason may be the biases of modeling the optical properties of
453 Martian dust, which is quite experimental in the current version of the model. The deficiency
454 in modeling dust optical properties and their radiative impact may lead to inconsistencies
455 between the assessment with T15 and CDOD.

456

457 3.2.2 Spatial variation

458 In addition to the seasonal variation, the spatial distribution of dust is also important.
459 Therefore, the simulated spatial distributions of dust are evaluated below. As shown by the
460 observed CDOD in Fig. 7a1, the dust amount increases significantly in the polar region of the
461 northern hemisphere near the summer solstice and is higher than that at the middle and low

462 latitudes. This may be because CO_2 ice sublimates, and a strong temperature gradient is
463 formed in the ice cap-non-ice cap regions near the edge of the Arctic ice cap, which enhances
464 the wind speed. The probability of dust lifted from the surface into the air is strengthened in
465 this region (James et al., 1999). However, the meridional distribution of dust in SL2 during
466 the summer solstice shows more dust at the low and middle latitudes and less dust at the high
467 latitudes, which is significantly different from the observations. SL3 also has such a
468 deficiency. It is worth noting that, whether using the current convective lifting scheme or
469 wind stress lifting scheme or even combining these two lifting schemes, the model cannot
470 reproduce the relatively high CDOD during the solstice in the polar regions.

471 To further assess the simulated spatial distribution of Martian dust, Figure 8 shows the
472 zonally averaged CDOD for the four seasons. In terms of magnitude, SL1 underestimates
473 dust, SL3 overestimates dust globally throughout the year, while SL2 produces much better
474 results than the LMD dataset (Figure 8a1-a4). Consistent with what is shown in Fig. 7, in
475 boreal spring and summer, the dust amount at the polar of the northern hemisphere in SL2 is
476 less than that observed, while the dust amount at the low and middle latitudes of the northern
477 hemisphere in SL2 is more than observed. In boreal autumn and winter, the dust amount in
478 the polar region of the northern hemisphere is significantly overestimated in SL2, while the
479 dust amount in the polar region of the southern hemisphere is underestimated. In boreal
480 winter, SL2 overestimates the dust amount at low and middle latitudes in both hemispheres.
481 It is worth noting that although SL3 significantly overestimates the magnitude of CDOD
482 globally, it produces a meridional distribution of CDOD similar to that of SL2 after
483 normalization (Fig. 8b1-b4). However, SL1, with a much lower amount of dust lifted globally,
484 produces a relatively higher dust amount at high latitudes in all seasons (peak in the southern
485 polar region in boreal summer and in the northern polar region in other seasons), which
486 indicates that tuning the threshold drag velocity can affect not only the simulated global mean
487 magnitude but also the spatial distribution of dust.

488 To further understand the different spatial distributions of normalized dust amounts
489 among the three experiments, the spatial and temporal variations of the drag velocity, the
490 threshold drag velocity, and the drag velocity averaged only for the time and space when it is
491 larger than the threshold are shown in Figure 9. The main difference among the three
492 experiments comes from their difference in threshold drag velocity, which is tuned
493 intentionally as discussed above. There is also some small difference in drag velocity among
494 the three experiments due to the feedback of changing dust amount on meteorological fields.

495 The results show a large threshold drag velocity and small drag velocity in SL1 throughout
496 the year (Fig. 9a1 and b1). The drag velocity is rarely larger than the threshold drag velocity
497 in SL1, only at middle and high latitudes in boreal autumn and winter. This indicates that the
498 normalized spatial variation in SL1 in summer (Fig. 8b2) is mainly due to the numerical
499 calculation without any physical meaning. With the decrease of the threshold drag velocity in
500 SL2 and SL3, the possibility of the drag velocity larger than the threshold drag velocity
501 increases significantly, especially in the mid-latitudes in spring and summer of the two
502 hemispheres, leading to the expansion of dust lifting areas and the increase of dust mass. The
503 tuning of the threshold drag velocity can affect the spatial distribution of dust until it reaches
504 a certain value with which the simulated normalized meridional distribution of dust tends to
505 be similar.

506 In terms of the underestimation (overestimation) of dust amount at high latitudes (mid
507 and low latitudes) in boreal spring and summer, part of the reason may be due to the
508 underestimation of dust amount lifted at high latitudes (Fig. 4). The strong temperature
509 gradient and hence the wind enhancement near the polar regions due to CO₂ ice sublimation
510 may not be well simulated in the model (Chow et al., 2022; Kahre et al., 2006). In a
511 sensitivity experiment (CAP), the wind stress lifting scheme is adjusted to increase the
512 probability of dust lifting at the edge of the CO₂ ice cap as a function of the change of ice cap,
513 and the bias of the spatial distribution of dust in boreal summer still cannot be reduced (Fig.
514 S3 in the supporting material). Further analysis of the spatial patterns of dust emissions and
515 mass loading (not shown) indicates that the bias may be related to biases not only in the dust
516 lifting scheme in boreal summer but also in the simulated circulation and dust transport. The
517 comparison of near-surface pressure and wind field between the simulations and the MCD
518 dataset is shown in Figure 10. In boreal summer, the spatial distribution of the wind field and
519 pressure in SL2 is quite different from that in the MCD dataset. The high-pressure center and
520 the corresponding clockwise wind circulation around the polar region in SL2 are opposite to
521 the low-pressure center and thus the counterclockwise wind rotation in the MCD dataset. It is
522 worth noting that even though there is more dust mass lifted at high latitudes in the sensitivity
523 experiment CAP, the spatial pattern of wind fields and pressure in CAP is similar to that in
524 SL2, which may be related to the numerical filtering in MarsWRF to deal with the decreasing
525 zonal grid at high latitudes (Toigo et al., 2012), which deserves further investigation.

526

527 **4. Summary and discussion**

528 The dust cycle plays an important role in the Martian atmosphere, and dust lifting is the
529 first step in the dust cycle processes by lifting surface dust into the air. Therefore, this study
530 focuses on the dust lifting schemes in the MarsWRF GCM. This model provides two widely
531 used dust lifting schemes: a convective lifting scheme and a wind stress lifting scheme. Since
532 the contributions of the two schemes are still uncertain, the ability of each scheme to simulate
533 the dust cycle is discussed, focusing on the seasonal magnitude and variation of Martian dust.

534 For the convective lifting scheme, this study focuses on the simulations of the dust cycle
535 by varying the lifting efficiency and assessing the simulations with the seasonal variation of
536 T15 and the frequency of dust devils. Compared with T15, the convective lifting scheme can
537 reproduce the seasonal variation of atmospheric temperature affected by dust regardless of
538 the change in lifting efficiency. The magnitude of T15 in CL2 is closer to the observation
539 data in the three experiments. This means that on Mars, the seasonal variation of global mean
540 Martian dust can be reproduced by applying the convective lifting scheme alone. However,
541 there are several problems with the simulated spatial distribution of dust devils compared
542 with the frequency of observed dust devils. First, this scheme simulates fewer dust devils in
543 northern Amazonis Planitia and cannot reproduce the phenomenon that the Martian dust devil
544 reaches its peak in this region. Second, there are fewer dust devils in the mid-latitudes of the
545 northern hemisphere and more dust devils in the southern hemisphere against the
546 observations. This suggests that the current convective lifting scheme is not appropriate for
547 simulating Martian dust, at least not based on sound physical mechanisms.

548 For the wind stress lifting scheme, this study focuses on simulations of the seasonal
549 magnitude and variation of dust by varying the threshold drag velocity. To evaluate the dust
550 lifting scheme more comprehensively, this study uses two metrics, T15 and CDOD, reflecting
551 atmospheric temperature and dust optical depth, respectively. SL2 with appropriately tuned
552 lifting efficiency and threshold drag velocity simulates the best magnitude of T15 against the
553 reanalysis data but overestimates the seasonal variation due to its positive bias of T15
554 magnitude in boreal winter. However, SL2 can reproduce the seasonal magnitude and
555 variation of CDOD well against the reanalysis. This discrepancy in the assessment with T15
556 and CDOD may be partly due to the observational uncertainties related to T15 and CDOD
557 and the biases of experimentally modeling the optical properties and radiative feedback of
558 Martian dust in the current model, which deserves further investigation. Overall, it is possible
559 to reproduce the seasonal magnitude and variation of global mean atmospheric temperature
560 and CDOD using the wind stress lifting scheme only with appropriately tuned parameters,

561 except that the model still cannot capture the observed bimodal structure in boreal autumn
562 and winter, which needs to be improved in the future.

563 For the spatial distribution of dust simulated with the wind stress lifting process, the SL2
564 and SL3 experiments can generally simulate the meridional distribution of dust mass that
565 decreases from the low to high latitudes. Although SL2 can generally capture the seasonal
566 magnitude and variation of global mean dust amount, there are still significant biases in its
567 simulated spatial distribution of dust no matter how parameters are tuned, such as it
568 overestimates dust amount at low and middle latitudes in both hemispheres in boreal winter.
569 In addition, the simulations cannot capture the observed relatively high dust mass at high
570 latitudes than at low and middle latitudes (boreal summer for the northern hemisphere and
571 boreal winter for the southern hemisphere) that may be due to local dust storms occurring
572 frequently at the cap edges of CO_2 ice in both hemispheres. The sensitivity experiments and
573 analysis indicate that the biases in large-scale atmospheric circulation, particularly at high
574 latitudes, may also contribute to the underestimation of dust over polar regions. Please note
575 that these modeling biases in spatial distribution cannot be mitigated with the combination of
576 current convective lifting and wind stress lifting schemes. The results also indicate that
577 tuning the threshold drag velocity can affect not only the simulated global mean magnitude
578 but also the spatial distribution of dust.

579 There are some limitations in the assessment of this study. This study focuses on the
580 impact of the dust lifting process on the spatial and temporal distributions of atmospheric
581 dust, ignoring to discuss many other processes that affect dust distributions, such as
582 sedimentation, PBL mixing, sublimation of the CO_2 ice cap, and dust radiative feedback. In
583 addition, only one size of dust particle is used in the simulations. The influence of dust
584 particles simulated with more sizes needs to be assessed in the future. Due to the availability
585 of observations, this study uses only two metrics, T15 and CDOD, to evaluate the dust lifting
586 schemes. Directly observed or retrieved dust lifting fluxes and vertical distributions of dust
587 properties would be very helpful for further understanding the Martian dust cycle and
588 improving Martian dust modeling.

589

590 **Data Availability Statement**

591 The reconstructed column dust optical depth based on Montabone et al. (2015) are freely
592 download at http://www-mars.lmd.jussieu.fr/mars/dust_climatology/index.html. The Mars
593 Climate Database outputs used in this study can be obtained from

594 <https://doi.org/10.5281/zenodo.7437175>. The MarsWRF model outputs are available at
595 <https://doi.org/10.5281/zenodo.7437972>.

596

597 **Author contributions**

598 Lulu Li and Chun Zhao designed the experiments and conducted and analyzed the
599 simulations. All authors contributed to the discussion and final version of the paper.

600

601 **Acknowledgments**

602 This research was supported by the Strategic Priority Research Program of Chinese Academy
603 of Sciences (grant XDB41000000), the National Key Research and Development Program of
604 China (2016YFA0602001), the National Natural Science Foundation of China (42061134009,
605 41775146), the Fundamental Research Funds for the Central Universities, the USTC
606 Research Funds of the Double First-Class Initiative, and the study used the computing
607 resources from the High-Performance Computing Center of University of Science and
608 Technology of China (USTC) and the TH-2 of National Supercomputer Center in Guangzhou
609 (NSCC-GZ).

610

611 **References**

- 612 Bagnold, R. A. (1974). The Physics of Blown Sand and Desert. *Methuen, New York*.
- 613 Basu, S., Richardson, M. I., & Wilson, R. J. (2004). Simulation of the Martian dust cycle with
614 the GFDL Mars GCM. *Journal of Geophysical Research: Planets*, 109(E11).
- 615 Basu, S., Wilson, J., Richardson, M., & Ingersoll, A. (2006). Simulation of spontaneous and
616 variable global dust storms with the GFDL Mars GCM. *Journal of Geophysical
617 Research*, 111(E9).
- 618 Bertrand, T., Wilson, R. J., Kahre, M. A., Urata, R., & Kling, A. (2020). Simulation of the 2018
619 global dust storm on Mars using the NASA Ames Mars GCM: a multitracer approach.
620 *Journal of Geophysical Research: Planets*, 125(7), e2019JE006122.
- 621 Cantor, B., Malin, M., & Edgett, K. S. (2002). Multiyear Mars Orbiter Camera (MOC)
622 observations of repeated Martian weather phenomena during the northern summer
623 season. *Journal of Geophysical Research: Planets*, 107(E3), 3-1-3-8.
- 624 Cantor, B. A. (2007). MOC observations of the 2001 Mars planet-encircling dust storm.
625 *Icarus*, 186(1), 60-96.
- 626 Cantor, B. A., James, P. B., & Calvin, W. M. (2010). MARCI and MOC observations of the
627 atmosphere and surface cap in the north polar region of Mars. *Icarus*, 208(1), 61-81.
- 628 Cantor, B. A., James, P. B., Caplinger, M., & Wolff, M. J. (2001). Martian dust storms: 1999
629 Mars orbiter camera observations. *Journal of Geophysical Research: Planets*,
630 106(E10), 23653-23687.
- 631 Cantor, B. A., Kanak, K. M., & Edgett, K. S. (2006). Mars Orbiter Camera observations of
632 Martian dust devils and their tracks (September 1997 to January 2006) and
633 evaluation of theoretical vortex models. *Journal of Geophysical Research: Planets*,
634 111(E12), n/a-n/a.
- 635 Capen, C. F., & Martin, L. J. (1971). The developing stages of the Martian yellow storm of
636 1971. *Lowell Observatory Bulletin*, 7, 211-216.
- 637 Chow, K.-C., Xiao, J., & Wang, Y.-M. (2022). Simulation of dust activities in the southern high
638 latitudes of Mars. *Planetary and Space Science*, 217.
- 639 Fenton, L. K., & Richardson, M. I. (2001). Martian surface winds: Insensitivity to orbital
640 changes and implications for aeolian processes. *Journal of Geophysical Research:
641 Planets*, 106(E12), 32885-32902.
- 642 Fisher, J. A., Richardson, M. I., Newman, C. E., Szwast, M. A., Graf, C., Basu, S., et al. (2005).
643 A survey of Martian dust devil activity using Mars Global Surveyor Mars Orbiter
644 Camera images. *Journal of Geophysical Research: Planets*, 110(E3).
- 645 Forget, F., Hourdin, F., Fournier, R., Hourdin, C., Talagrand, O., Collins, M., et al. (1999).
646 Improved general circulation models of the Martian atmosphere from the surface to
647 above 80 km. *Journal of Geophysical Research: Planets*, 104(E10), 24155-24175.
- 648 Garratt, J. R. (1994). THE ATMOSPHERIC BOUNDARY-LAYER - REVIEW. *Earth-Science Reviews*,
649 37(1-2), 89-134. <Go to ISI>://WOS:A1994PN31900002
- 650 Gierasch, P., & Goody, R. (1968). A study of the thermal and dynamical structure of the
651 Martian lower atmosphere. *Planetary and Space Science*, 16(5), 615-646.
- 652 Gierasch, P., & Goody, R. (1972). The effect of dust on the temperature of the Martian
653 atmosphere. *Journal of the Atmospheric Sciences*, 29(2), 400-402.
- 654 Greeley, R., & Iversen, J. D. (1987). *Wind as a geological process: on Earth, Mars, Venus and
655 Titan*: CUP Archive.

656 Guzewich, S. D., Toigo, A. D., Richardson, M. I., Newman, C. E., Talaat, E. R., Waugh, D. W., &
657 McConnochie, T. H. (2013). The impact of a realistic vertical dust distribution on the
658 simulation of the Martian General Circulation. *Journal of Geophysical Research:*
659 *Planets*, 118(5), 980-993.

660 Haberle, R. M., Clancy, R. T., Forget, F., Smith, M. D., & Zurek, R. W. (2017). *The atmosphere*
661 *and climate of Mars*: Cambridge University Press.

662 Haberle, R. M., Leovy, C. B., & Pollack, J. B. (1982). Some effects of global dust storms on the
663 atmospheric circulation of Mars. *Icarus*, 50(2-3), 322-367.

664 Hinson, D., & Wilson, R. (2002). Transient eddies in the southern hemisphere of Mars.
665 *Geophysical Research Letters*, 29(7), 58-51-58-54.

666 James, P. B., Hollingsworth, J. L., Wolff, M. J., & Lee, S. W. (1999). North polar dust storms in
667 early spring on Mars. *Icarus*, 138(1), 64-73.

668 Kahre, M. A., Murphy, J. R., & Haberle, R. M. (2006). Modeling the Martian dust cycle and
669 surface dust reservoirs with the NASA Ames general circulation model. *Journal of*
670 *Geophysical Research-Planets*, 111(E6). <Go to ISI>://WOS:000238572200001

671 Kahre, M. A., Murphy, J. R., Newman, C. E., Wilson, R. J., Cantor, B. A., Lemmon, M. T., et al.
672 (2017). The Mars Dust Cycle. In *The Atmosphere and Climate of Mars* (pp. 295-337).

673 Madeleine, J. B., Forget, F., Millour, E., Montabone, L., & Wolff, M. J. (2011). Revisiting the
674 radiative impact of dust on Mars using the LMD Global Climate Model. *Journal of*
675 *Geophysical Research-Planets*, 116. <Go to ISI>://WOS:000297419600003

676 McKim, R. (1999). Meeting contribution: recent views of Mars. *Journal of the British*
677 *Astronomical Association*, 109, 287.

678 Merrison, J., Gunnlaugsson, H., Nørnberg, P., Jensen, A., & Rasmussen, K. (2007).
679 Determination of the wind induced detachment threshold for granular material on
680 Mars using wind tunnel simulations. *Icarus*, 191(2), 568-580.

681 Montabone, L., Forget, F., Millour, E., Wilson, R. J., Lewis, S. R., Cantor, B., et al. (2015).
682 Eight-year climatology of dust optical depth on Mars. *Icarus*, 251, 65-95.

683 Newman, C. E., Lewis, S. R., & Read, P. L. (2005). The atmospheric circulation and dust
684 activity in different orbital epochs on Mars. *Icarus*, 174(1), 135-160.

685 Newman, C. E., Lewis, S. R., Read, P. L., & Forget, F. (2002a). Modeling the Martian dust
686 cycle 2. Multiannual radiatively active dust transport simulations. *Journal of*
687 *Geophysical Research: Planets*, 107(E12), 7-1-7-15.

688 Newman, C. E., Lewis, S. R., Read, P. L., & Forget, F. (2002b). Modeling the Martian dust
689 cycle, 1. Representations of dust transport processes. *Journal of Geophysical*
690 *Research: Planets*, 107(E12), 6-1-6-18.

691 Newman, C. E., & Richardson, M. I. (2015). The impact of surface dust source exhaustion on
692 the martian dust cycle, dust storms and interannual variability, as simulated by the
693 MarsWRF General Circulation Model. *Icarus*, 257, 47-87.

694 Pollack, J. B., Haberle, R., Greeley, R., & Iversen, J. (1976). Estimates of the wind speeds
695 required for particle motion on Mars. *Icarus*, 29(3), 395-417.

696 Pollack, J. B., Haberle, R. M., Schaeffer, J., & Lee, H. (1990). Simulations of the general
697 circulation of the Martian atmosphere: 1. Polar processes. *Journal of Geophysical*
698 *Research: Solid Earth*, 95(B2), 1447-1473.

699 Rennó, N. O., Burkett, M. L., & Larkin, M. P. (1998). A simple thermodynamical theory for
700 dust devils. *Journal of Atmospheric Sciences*, 55(21), 3244-3252.

701 Richardson, M. I., Toigo, A. D., & Newman, C. E. (2007). PlanetWRF: A general purpose, local
702 to global numerical model for planetary atmospheric and climate dynamics. *Journal*

703 of *Geophysical Research: Planets*, 112(E9).
704 <https://agupubs.onlinelibrary.wiley.com/doi/abs/10.1029/2006JE002825>
705 Thomas, P., & Gierasch, P. J. (1985). Dust devils on Mars. *Science*, 230(4722), 175-177.
706 Toigo, A. D., Lee, C., Newman, C. E., & Richardson, M. I. (2012). The impact of resolution on
707 the dynamics of the martian global atmosphere: Varying resolution studies with the
708 MarsWRF GCM. *Icarus*, 221(1), 276-288.
709 Toigo, A. D., Richardson, M. I., Wang, H., Guzewich, S. D., & Newman, C. E. (2018). The
710 cascade from local to global dust storms on Mars: Temporal and spatial thresholds
711 on thermal and dynamical feedback. *Icarus*, 302, 514-536.
712 Viúdez - Moreiras, D., Newman, C., De la Torre, M., Martínez, G., Guzewich, S., Lemmon,
713 M., et al. (2019). Effects of the MY34/2018 global dust storm as measured by MSL
714 REMS in Gale Crater. *Journal of Geophysical Research: Planets*, 124(7), 1899-1912.
715 Wang, Y., Chow, K.-C., Xiao, J., & Wong, C.-F. (2021). Effect of dust particle size on the
716 climate of Mars. *Planetary and Space Science*, 208.
717 Westphal, D. L., Toon, O. B., & Carlson, T. N. (1987). A two - dimensional numerical
718 investigation of the dynamics and microphysics of Saharan dust storms. *Journal of*
719 *Geophysical Research: Atmospheres*, 92(D3), 3027-3049.
720 Whelley, P. L., & Greeley, R. (2006). Latitudinal dependency in dust devil activity on Mars.
721 *Journal of Geophysical Research*, 111(E10).
722 Whelley, P. L., & Greeley, R. (2008). The distribution of dust devil activity on Mars. *Journal of*
723 *Geophysical Research: Planets*, 113(E7).
724 White, B. R. (1979). Soil transport by winds on Mars. *Journal of Geophysical Research: Solid*
725 *Earth*, 84(B9), 4643-4651.
726 Wu, Z., Li, T., Heavens, N. G., Newman, C. E., Richardson, M. I., Yang, C., et al. (2022). Earth-
727 like thermal and dynamical coupling processes in the Martian climate system. *Earth-*
728 *Science Reviews*, 229.
729 Wu, Z., Richardson, M. I., Zhang, X., Cui, J., Heavens, N. G., Lee, C., et al. (2021). Large Eddy
730 Simulations of the Dusty Martian Convective Boundary Layer With MarsWRF. *Journal*
731 *of Geophysical Research: Planets*, 126(9).
732 Xiao, J., Chow, K.-C., & Chan, K.-I. (2019). Dynamical processes of dust lifting in the northern
733 mid-latitude region of Mars during the dust storm season. *Icarus*, 317, 94-103.
734 Zurek, R. W., & Martin, L. J. (1993). Interannual variability of planet - encircling dust storms
735 on Mars. *Journal of Geophysical Research: Planets*, 98(E2), 3247-3259.
736
737

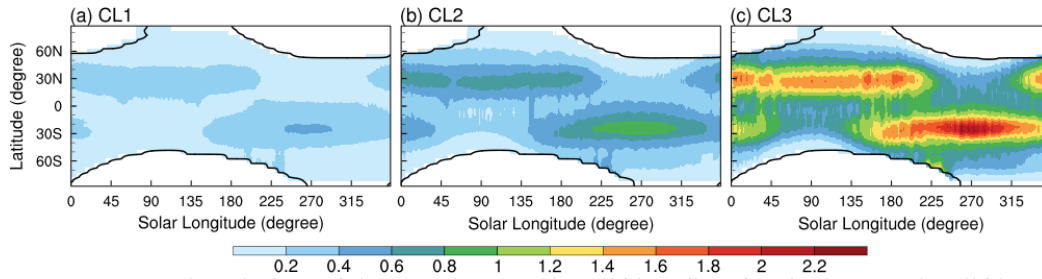
738
739
740
741
742
743
744
745

Table 1. Numerical experiments in this study.

Experiment	α_{CL} ($10^{-9} \text{ kg J}^{-1}$)	α_{SL} (10^{-7} m^{-1})	β	Cap affect
CL1	1	-	-	-
CL2	3	-	-	-
CL3	10	-	-	-
SL1	-	5	1	-
SL2	-	5	0.35	-
SL3	-	5	0.1	-
CAP	-	5	0.35	increase

746
747
748
749
750
751
752
753
754
755
756
757
758
759
760
761
762
763
764
765
766
767
768
769
770
771
772
773
774
775

776
777
778
779
780
781
782
783
784
785
786

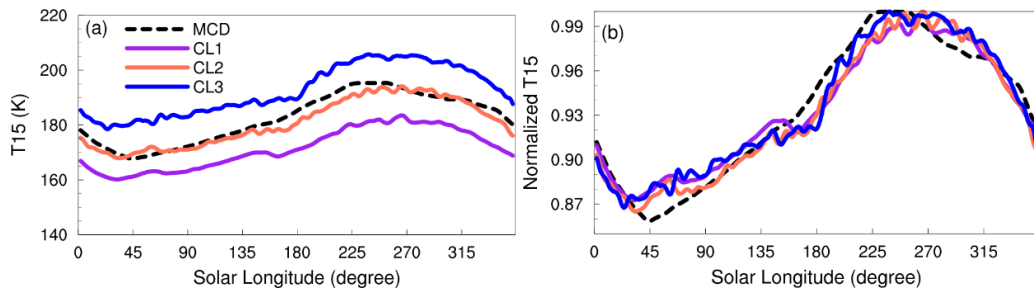


787
788

Figure 1. Seasonal variation of the zonal-mean dust lifting flux for the convective lifting scheme (shaded, $10^{-7} \text{ kg/m}^2/\text{s}$). (a) CL1; (b) CL2; (c) CL3. The black contours depict the edges of CO_2 ice cap.

790
791
792
793
794
795
796
797
798
799
800
801
802
803
804
805
806
807
808

809
810
811
812
813
814
815
816
817



818

819 **Figure 2.** The seasonal variation of (a) the mid-level layer atmospheric temperature (T15)
820 between $40^{\circ}S$ and $40^{\circ}N$ (in units of K); (b) normalized T15. The dashed line indicates the
821 T15 in MCD, and the solid lines indicate the MarsWRF model simulation. The purple line is
822 simulation CL1, the orange line is simulation CL2, and the blue line is simulation CL3.

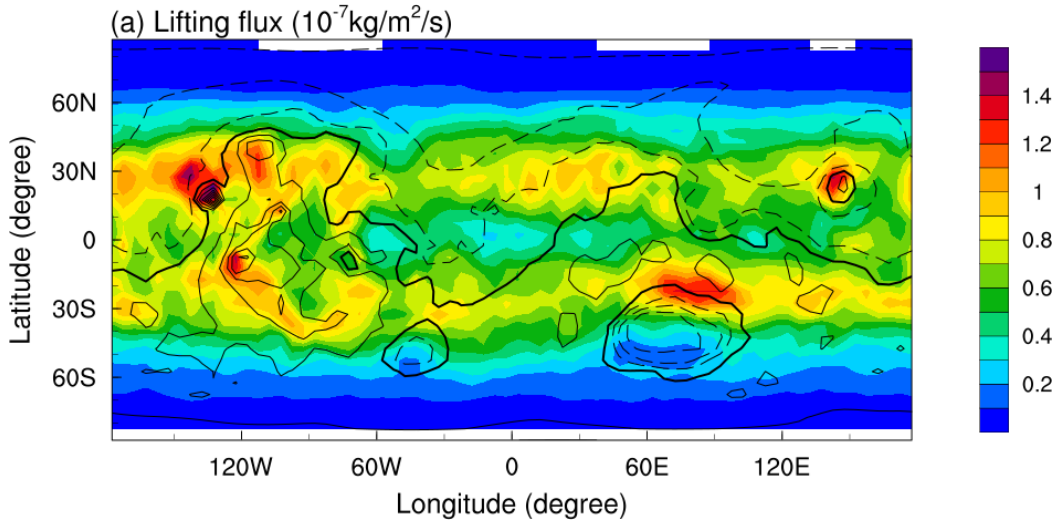
823
824
825
826
827
828
829
830
831
832
833
834
835
836
837

838

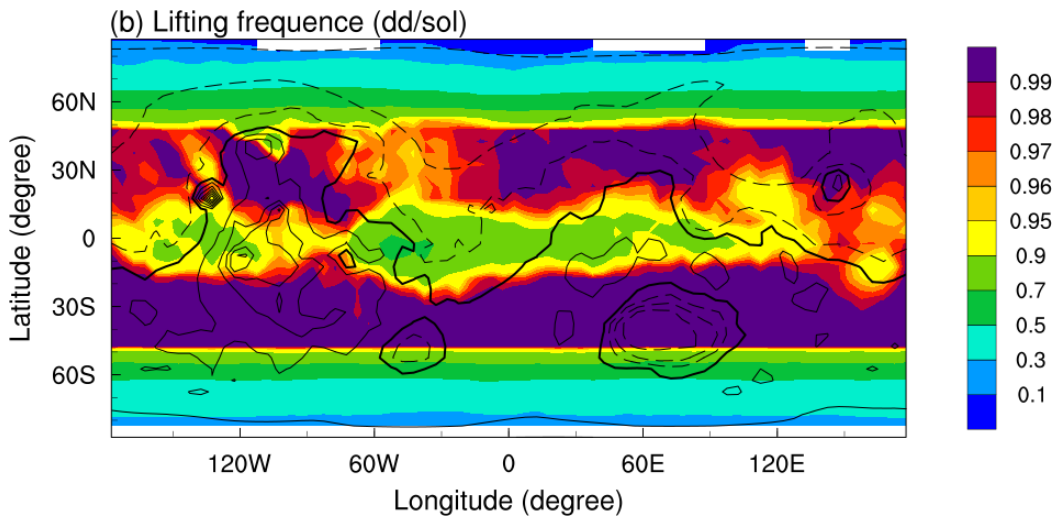
839

840

841



842



843

844 **Figure 3.** Spatial distribution of convective lifting averaged over the year at 14 pm. (a) Dust
845 lifting flux (shaded, $10^{-7} \text{kg/m}^2/\text{s}$); (b) lifting frequency (dd/sol), equivalent to the
846 occurrence frequency of dust devils in the model; contour lines indicate terrain height at 2 km
847 intervals, solid lines are positive, dashed lines are negative.

848

849

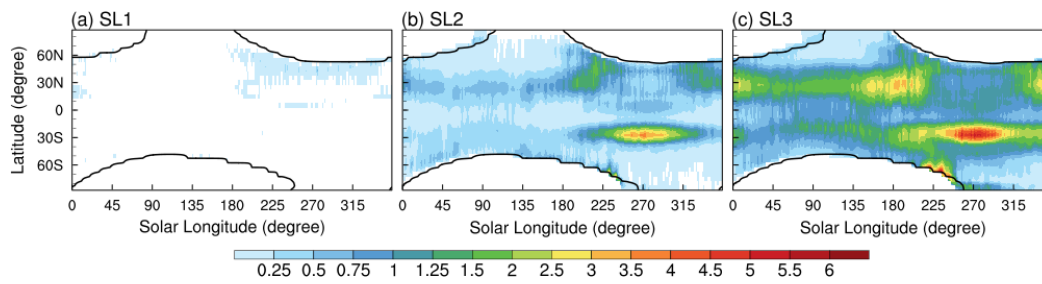
850

851

852

853

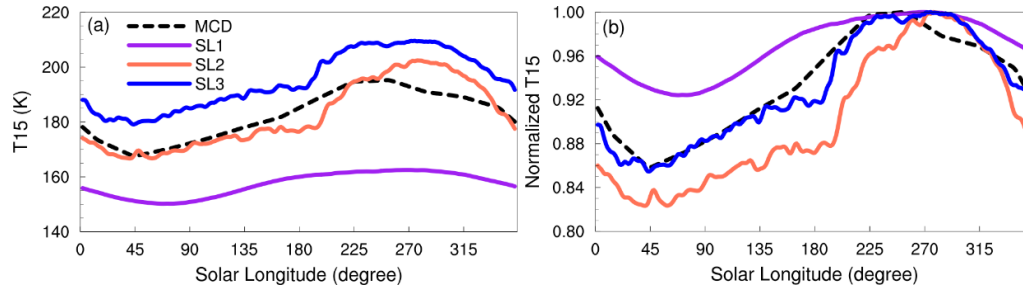
854
855
856
857
858
859
860
861
862



863
864
865
866
867
868
869
870
871
872
873
874
875
876
877
878
879
880
881
882
883

Figure 4. Same as Figure 1 but for the dust lifting flux (in units of $10^{-7} \text{ kg/m}^2/\text{s}$) from the wind stress lifting scheme.

884
885
886
887
888
889
890

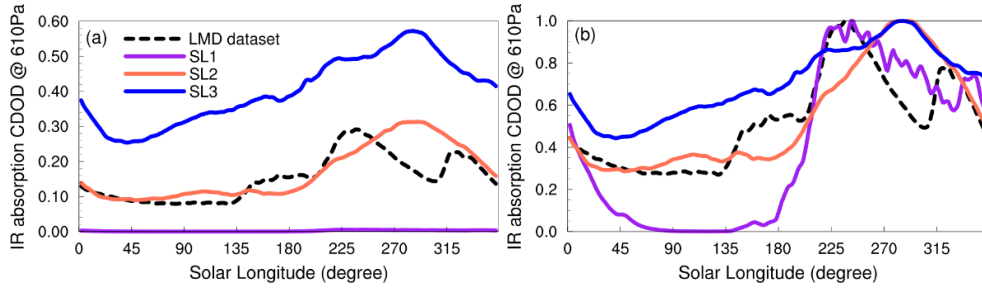


891

892 **Figure 5.** Same as Figure 2 but for the wind stress lifting scheme.

893
894
895
896
897
898
899
900
901
902
903
904
905
906
907
908
909
910
911
912

913
914
915
916
917
918
919

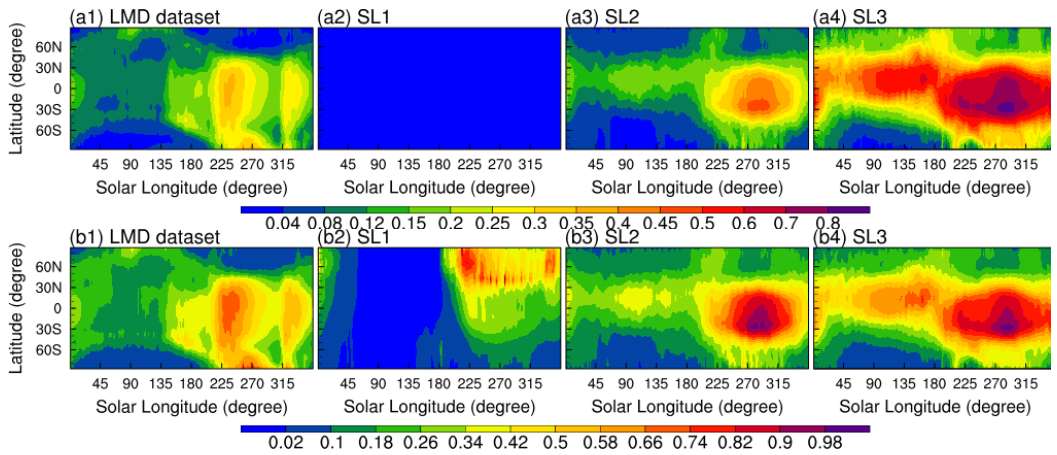


920

921 **Figure 6.** Temporal distribution of (a) the global average column dust optical depth in the
922 infrared band at 610 Pa; (b) normalized IR absorption CDOD at 610 Pa. The dashed line
923 indicates observations, and the solid lines indicate the MarsWRF model simulation. The
924 black dashed line shows the reconstructed observation data of CDOD averaged for eight
925 years from 24 to 34 excluding MY25, MY28 and MY34 when containing global dust storms
926 (Montabone et al., 2015). The purple line is simulation SL1, the orange line is simulation SL2,
927 and the blue line is simulation SL3.

928
929
930
931
932
933
934
935
936
937
938
939
940
941
942
943
944
945
946
947

948
 949
 950
 951
 952
 953
 954
 955

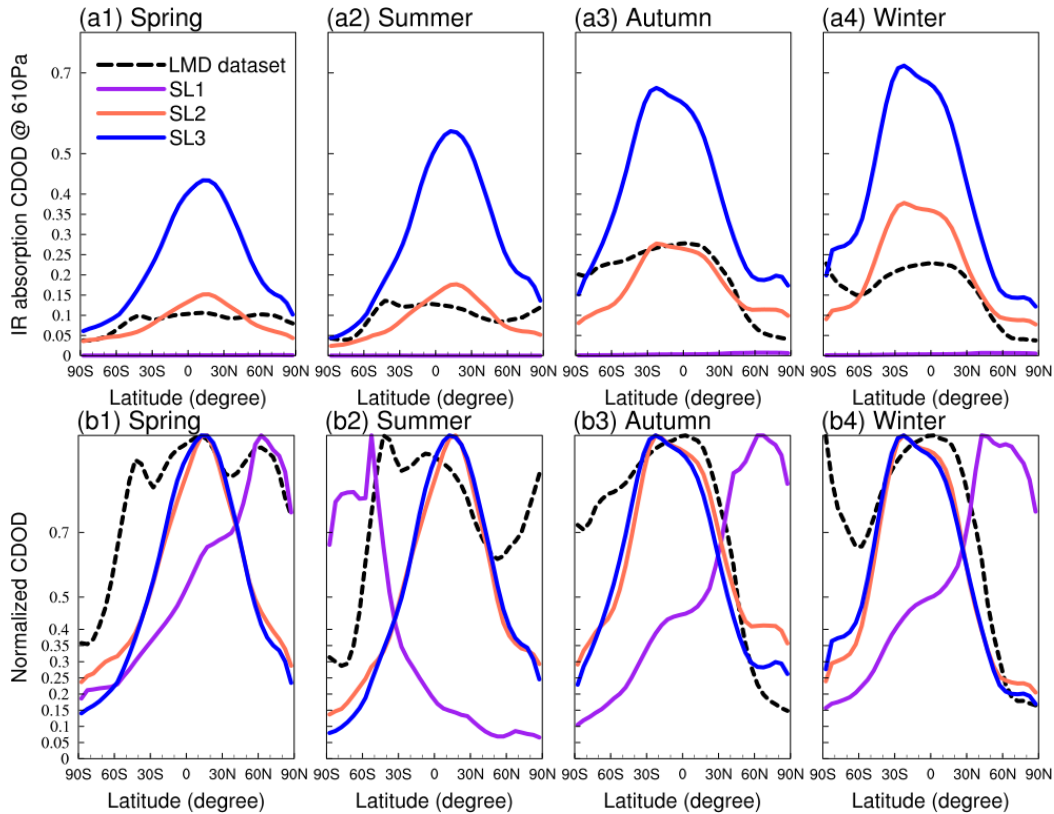


956

957
 958
 959
 960
 961
 962
 963
 964
 965
 966
 967
 968
 969
 970
 971
 972
 973
 974
 975
 976
 977
 978
 979
 980
 981
 982
 983
 984
 985

Figure 7. Seasonal variation of zonal-mean IR absorption CDOD at 610 Pa (shaded, upper panel) and normalized CDOD (shaded, lower panel). From left to right are the LMD data excluding three years with global dust storms, SL1, SL2 and SL3.

986
987
988
989
990
991
992
993



994

995

996

Figure 8. Zonally averaged CDOD for the four seasons (a1-a4) and normalized (b1-b4).
997 Numbers from 1 to 4 correspond to spring, summer, autumn and winter. LMD dataset
998 (dashed line), SL1 (purple), SL2 (orange), SL3 (blue).
999

1000

1001

1002

1003

1004

1005

1006

1007

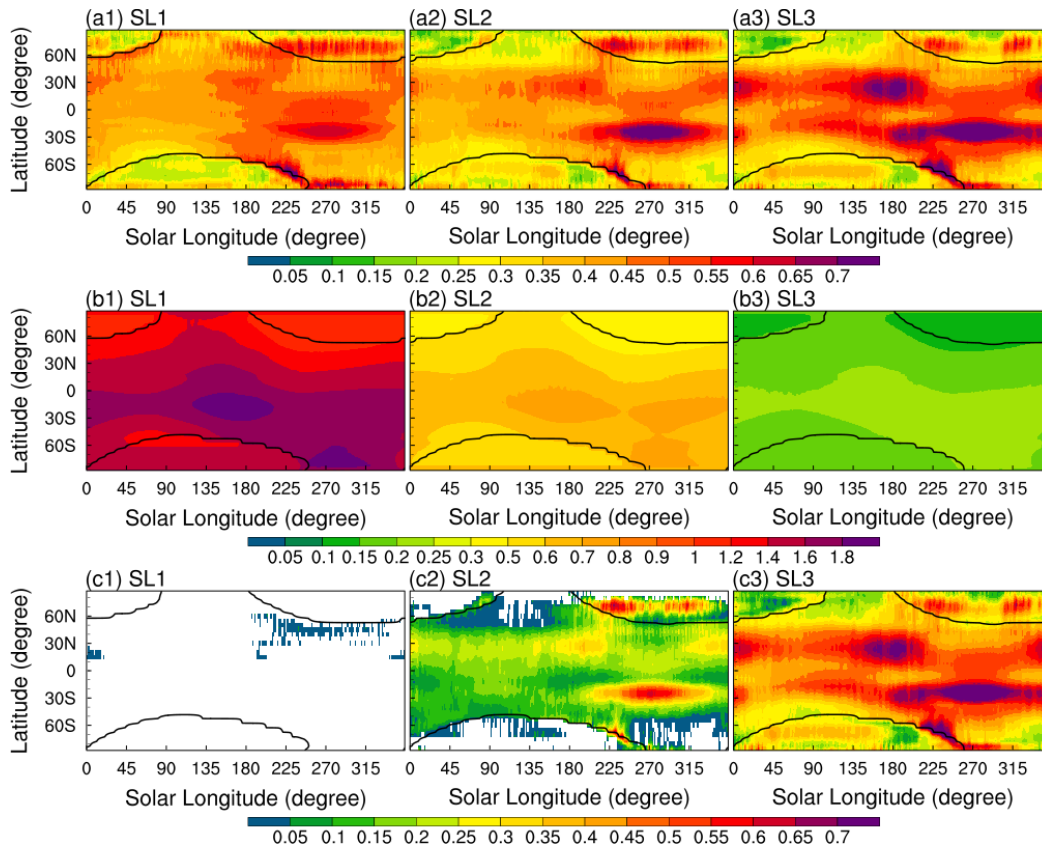
1008

1009

1010

1011

1012
1013
1014
1015
1016
1017



1018

1019

1020

1021

1022

1023

1024

1025

1026

1027

1028

1029

1030

1031

1032

1033

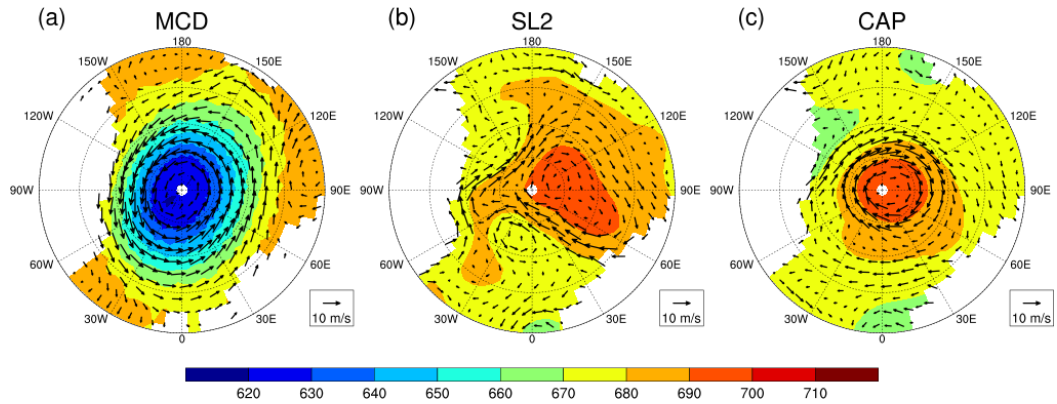
1034

1035

1036

Figure 9. Seasonal variation of the drag velocity (shaded, top panel), the threshold drag velocity (shaded, middle panel) and the drag velocity averaged for the time and space when it is larger than the threshold drag velocity (shaded, bottom panel), in units of m/s. From left to right are SL1, SL2 and SL3. The black contours depict the edge of the CO2 ice cap.

1037
1038
1039
1040
1041
1042
1043
1044
1045



1046
1047 **Figure 10.** The pressure (shaded, in units of Pa) and wind field (vectors, in units of m/s) near
1048 the surface in the polar projection of the northern hemisphere at $L_s = 90^\circ$; the outermost
1049 circle is $30^\circ N$. From left to right are the MCD, SL2 and CAP.
1050
1051
1052
1053
1054
1055
1056